Smart Window Structures Based on Highly Conductive, Transparent Metal Nanomeshes and Thermochromic Perovskite Films

Shang-Hsuan Wu, Gabriel Cossio, Benjamin Braun, Frances Camille M. Wu, and Edward T. Yu*

Smart windows are energy-efficient windows whose optical transparency can be switched between highly transparent and opaque states in response to incident solar illumination. Transparent and conductive metal nanomesh (NM) films are promising candidates for thermochromic smart windows due to their excellent thermal conductivity, high optical transparency at near infrared wavelengths, and outstanding stability. In this study, ZnO/Au/Al$_2$O$_3$ NM films with periodicities of 200 and 370 nm are reported. The ZnO/Au/Al$_2$O$_3$ NM film with a 370 nm periodicity exhibits a transmittance over 90% at 550 nm and sheet resistance lower than 20 Ω sq^{-1}. Based on a standard figure of merit, this structure outperforms current state-of-the-art NM films. Here, the integration of ZnO/Au/Al$_2$O$_3$ NM films into a thermochromic perovskite smart window is also demonstrated. The transparency of the smart window structure is manipulated by transient resistive heating to trigger the thermochromic transition to the opaque state, which can be then maintained solely by 1-sun, AM 1.5 G illumination. This climate-adaptive, low power-activated, and fast-switching smart window structure opens new pathways toward its practical application in the real world.

1. Introduction

Thermochromic smart windows are windows whose optical transparency changes reversibly from a transparent to an opaque state in response to heating, ideally by incident solar illumination.[1,2] Hybrid halide perovskites are promising candidates for thermochromic smart windows owing to their capability to undergo reversible color and phase transitions between low and high temperatures.[3,4] Recently, a new concept for smart photovoltaic windows has been realized based on inorganic perovskite CsPbI$_{3-x}$Br$_x$ thin films, which possess both photovoltaic and thermochromic features.[5] Transparent conductive electrodes (TCEs) are a key component in thermochromic smart windows, serving as both electrical

conductors and transparent heaters for the activation of thermochromism.[6,7] Low resistance and high transparency of TCEs are two essential prerequisites for a variety of applications, including the fabrication of smart windows.[8] Among various TCEs, highly transparent and conductive indium tin oxide (ITO) is most commonly employed; however, its highly brittle nature hinders its application in flexible electronics and the scarcity of indium results in high material cost.[9] The bending strain tolerance and mechanical flexibility of ITO/elastomeric substrates are inadequate because of the brittle nature of ITO, which renders flexible ITO substrates impractical for real-life stretchable, foldable, or bendable optoelectronics applications.[10] In addition, the relatively low thermal conductivity of ITO leads to longer response times for devices reliant on thermally activated transitions, such as thermochromic smart windows.

Extensive research has therefore been devoted to ITO alternatives including carbon-based TCEs such as graphene,[11] carbon nanotubes,[12] or conducting polymers,[13] and metal-based TCEs such as metal nanowires[14] or metal meshes.[15] Among these ITO alternatives, metal meshes, which are composed of periodic micro- or nanostructured metal networks on a transparent substrate, have gained considerable attention as high performance TCEs offering several advantages, including excellent mechanical flexibility, high conductivity, tunable transmittance, and low fabrication cost.[16,17] The current fabrication methods for these metal mesh films often involve low throughput, small-scale fabrication techniques such as e-beam lithography, nanoimprint lithography, photolithography, and laser writing, which are generally time-consuming and require substantial capital investment. Therefore, the nanosphere lithography method which involves a scalable, high throughput fabrication process of metal mesh films was introduced.[18]

Nanosphere lithography (NSL) enables rapid, low-cost fabrication of deep submicron metal nanomesh (NM) patterns via the self-assembled formation of a hexagonal close packed monolayer of spherical particles which serves as a patterning mask. It provides a scalable and high throughput lithography process which can be implemented for both rigid and flexible substrates.[19] Moreover, NSL enables precise control over the

S.-H. Wu, G. Cossio, B. Braun, F. C. M. Wu, E. T. Yu
Microelectronics Research Center
Department of Electrical and Computer Engineering
The University of Texas at Austin
Austin, TX 78758, USA
E-mail: ety@ece.utexas.edu

patterned hole nanostructure dimension in a metal mesh with high uniformity over large areas, enabling their potential application as high-performance transparent conductive electrodes. Recent advances in large-scale NSL methods based on roll-to-roll Langmuir Blodgett technique[20,21] and micropropulsive injection (MPI) method have been reported.[22,23] The developed MPI method could successfully yield a highly ordered monolayer of polystyrene (PS) spheres on different rigid or flexible substrates over very large areas (m^2).

One key concern for the development of metal mesh films in optoelectronic devices is their limited transmittance (less than ≈80%) due to the unavoidable opaque metal that covers a substantial part of the total area.[16] Another factor is the significant trade-off between the transmittance and sheet resistance values of metal mesh films. To date, the current state-of-the-art metal mesh films with high device performance are based on metal mesh patterns with relatively large pitch size. Bley et al. have demonstrated a process to fabricate hierarchical micro/nanohole arrays to create Au NM films consisting of regularly ordered large holes superimposed onto an array of smaller holes, resulting in transmittance (at 550 nm) and sheet resistance values of 82% and 71.6 Ω sq^{-1}, respectively with periodicity of 560 nm.[24] Qiu et al. have established trilayer NM films consisting of TiO$_2$/Au/TiO$_2$ multilayers, yielding transmittance (at 550 nm) and resistance values of 88.4% and 30 Ω sq^{-1}, respectively with periodicity of 650 nm.[25] In spite of these significant advancements in device performance, the large pitch size in many metal mesh films (560 and 650 nm) could hinder their potential application in optoelectronic devices due to, for example, increased charge carrier recombination in photovoltaic devices with short minority carrier diffusion lengths and high haze factor values in touch panels, displays, and smart windows.[24] In such cases, highly conductive and transparent metal mesh films with smaller periodicity (less than ≈380 nm) are desirable.

For perovskite-based thermochromic smart window devices, a configuration based on a metal mesh transparent heater integrated with a perovskite thermochromic layer is needed for the activation of thermochromism, which requires a relatively high transition temperature (>50 °C). Several studies have addressed the UV degradation of the perovskite layer which could lead to the release of volatile I$_2$ and CH$_3$NH$_3$I (MAI) from perovskite structure.[26,27] Additionally, Shlenskaya et al. discovered that the UV-induced precipitation of I$_2$ and MAI would further form a new (MA)$_2$Au$_2$I$_6$ phase in the perovskite film which is in direct contact with Au thin film.[28] Therefore, a thin, wide bandgap (3.2–3.4 eV) metal oxide material as a synergistic protective layer needs to be incorporated in between metal mesh and perovskite layers to improve the photo- and chemical-stability of thermochromic smart window devices. Among the wide bandgap metal oxide materials, ZnO is considered as a promising UV protective layer for perovskite layer due to its suitable optical bandgap (3.28 eV) and photostability under UV light.[29,30] While TiO$_2$ is another common UV blocking material, its sensitivity to UV irradiation results in the formation of radical species which could be a potential degradation source for the perovskite material.[31,32]

In this study, we introduce a new class of dielectric/dielectric NM films based on ZnO/Au/Al$_2$O$_3$ with periodicities

of 200 nm and 370 nm which are fabricated using NSL. For the metal mesh film design, an Au (15 nm) thin film is chosen as the electrode material due to its malleability and high electrical conductivity. Thin layers of Al$_2$O$_3$ film (20 nm) and ZnO film (20 nm) are used as high refractive index dielectric layers to induce antireflective effect and suppress surface plasmons. We use relatively smaller metal mesh periodicities of 200 and 370 nm as compared to previously reported trilayer NM films[25] to create a potential pathway to optoelectronic applications, such as smart windows, that often include nonsingle crystal semiconductors without sacrificing the overall device transmittance and sheet resistance. As a result, the ZnO/Au/Al$_2$O$_3$ NM film with a 370 nm periodicity exhibits transmittance over 90% at 550 nm which is the highest reported value based on our knowledge for these types of dielectric/metal/dielectric structures, and a sheet resistance lower than 20 Ω sq^{-1}. Thus, the overall device performance is superior to current state-of-the-art NM films and qualifies to compete with ITO glasses. Moreover, we extended this work to fabricate thermochromic perovskite (TC-PVK) smart windows that operate by inducing a thermochromic transition from transparent to opaque state via electrical heating of ZnO/Au/Al$_2$O$_3$ at 50 °C, which can be then maintained solely by 1-sun AM 1.5G illumination.

2. Results and Discussion

2.1. Fabrication and Structural Characterization of ZnO/Au/Al$_2$O$_3$ Nanomesh Films

ZnO/Au/Al$_2$O$_3$ NM films were prepared using the NSL method for patterning as illustrated schematically in **Figure 1**. Briefly, a self-assembled monolayer of PS nanospheres, either 200 nm or 370 nm in diameter, was formed using sequential injection via a pipette tip of colloidal PS nanospheres to the air-water interface of an aqueous reservoir, creating a hexagonal close packed monolayer on the water surface.[23] The self-assembled monolayer was then deposited onto a glass substrate by draining the reservoir and air-drying at room temperature overnight. Afterwards, the deposited PS nanospheres were partially etched by reactive ion etching (RIE) using an O$_2$ plasma process to reduce the diameter of PS spheres by approximately 20–40%. It has been reported that the etching rate and reactive gas composition influence the anisotropic shape and surface morphology of the PS nanosphere masks,[33] and etch conditions were optimized to create a spherical PS mask while reducing the sphere diameter. Next, 20 nm of Al$_2$O$_3$ and then 15 nm of Au were deposited on the nanosphere patterned surface using electron beam evaporation. The nanosphere masks were then lifted-off in order to form an Au/Al$_2$O$_3$ NM film. Finally, a ZnO sol-gel precursor was deposited onto the Au/Al$_2$O$_3$ NM film by spin coating and annealed at 200 °C for 30 min to create the final ZnO/Au/Al$_2$O$_3$ NM configuration.

For the creation of highly conductive and transparent metal mesh films, the two essential factors that need to be considered are the distance between adjacent etched spheres required to create a highly conductive periodic metal network and the size of the holes required to maximize the optical transparency, both of which are determined by the final etched sphere diameter.[33]
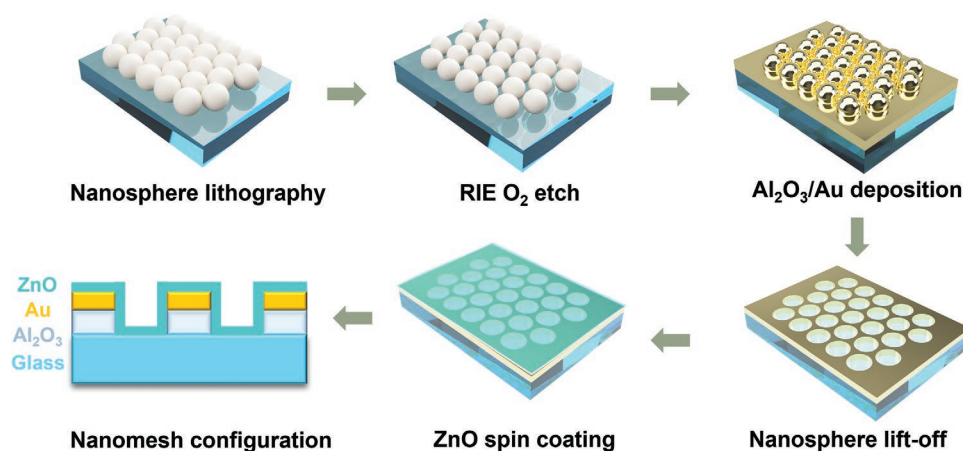
ADVANCED
SCIENCE NEWS
www.advancedsciencenews.com

ADVANCED
OPTICAL
MATERIALS
www.advopticalmat.de

Figure 1. Schematic illustration of the fabrication process for ZnO/Au/Al$_2$O$_3$ NM films.

15 nm Au was determined to be the optimum thickness of the conductive Au film, as greater thickness would reduce transparency while a reduction in the Au thickness would result in metal discontinuity, as described by Volmer–Weber mechanism, and consequently large sheet resistances.[34] The total thickness of the deposited Au/Al$_2$O$_3$ (15 nm/20 nm) NM film was optimized based on our smallest 200 nm PS spherical mask size. When the total thickness is greater than 35 nm, the lift-off process is typically unsuccessful, which we attribute to a tendency for the etched PS spheres to be buried under these thicker layers of deposited material, making lift off process difficult. **Figure 2**a,b show typical scanning electron microscopy (SEM) images of the ZnO/Au/Al$_2$O$_3$ NM fabricated using 200 and 370 nm NSL, respectively. After the lift-off process, the corresponding aperture diameters of 200 and 370 nm NSL ZnO/Au/Al$_2$O$_3$ NM films were determined from these SEM images, and decreased to 151 and 305 nm, respectively. Based on the SEM images, both periodicities (200 and 370 nm periodicity) exhibited highly ordered hexagonal nonclose packed NM patterns, confirming formation of high-quality nanoscale metal network. Figure 2c,d show atomic force microscopy (AFM) images and the corresponding height profiles (Figure 2e,f) of the ZnO/Au/Al$_2$O$_3$ NM films based on 200 and 370 nm NSL, respectively. The hole structures are highly circular, which can be attributed to a good optimization of the O$_2$ etching process for the PS nanospheres. The actual periodicities of the ZnO/Au/Al$_2$O$_3$ NM films fabricated using 200 and 370 nm NSL remained at 200 and 370 nm after the lift-off process. According to the AFM height profiles, average hole depths of ≈35 and ≈32 nm were observed on the 200 and 370 nm periodicity, respectively. These depth values were in good agreement with the combined thickness of the deposited 20 nm Al$_2$O$_3$ and 15 nm Au.
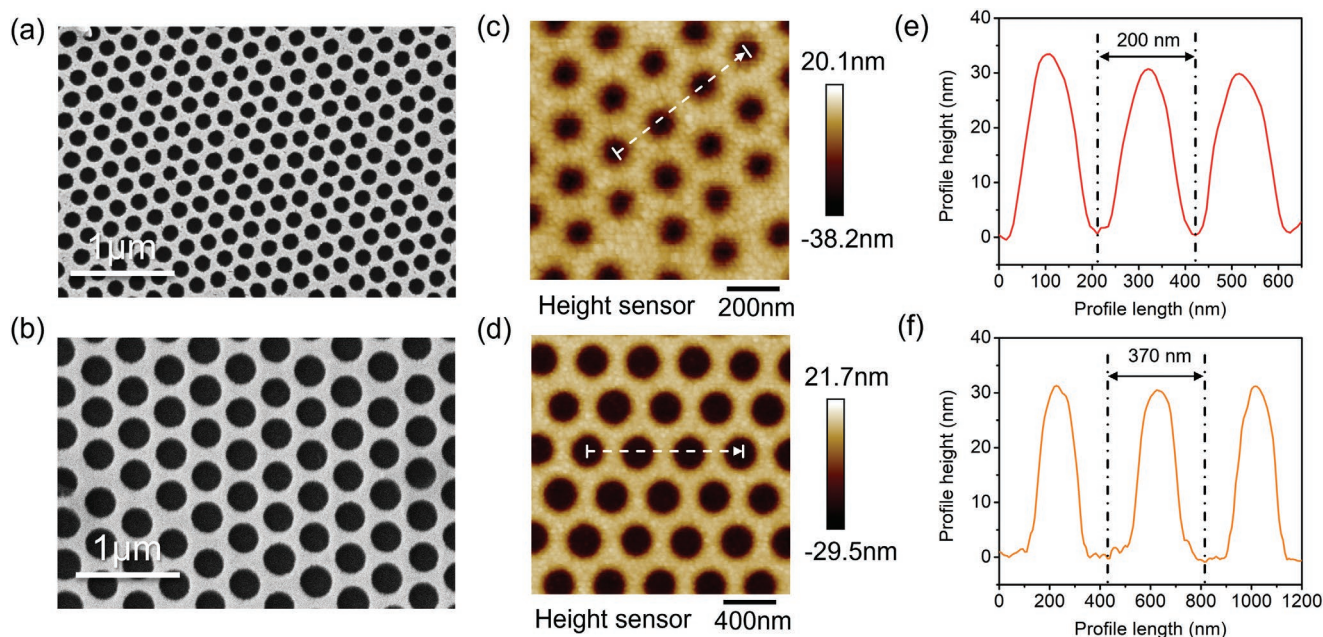

Figure 2. a,b) SEM images and c,d) AFM images with e,f) the corresponding line profile of ZnO/Au/Al$_2$O$_3$ NM films formed along 200 nm nanosphere diameter (top images) and 370 nm nanosphere diameter (bottom images).
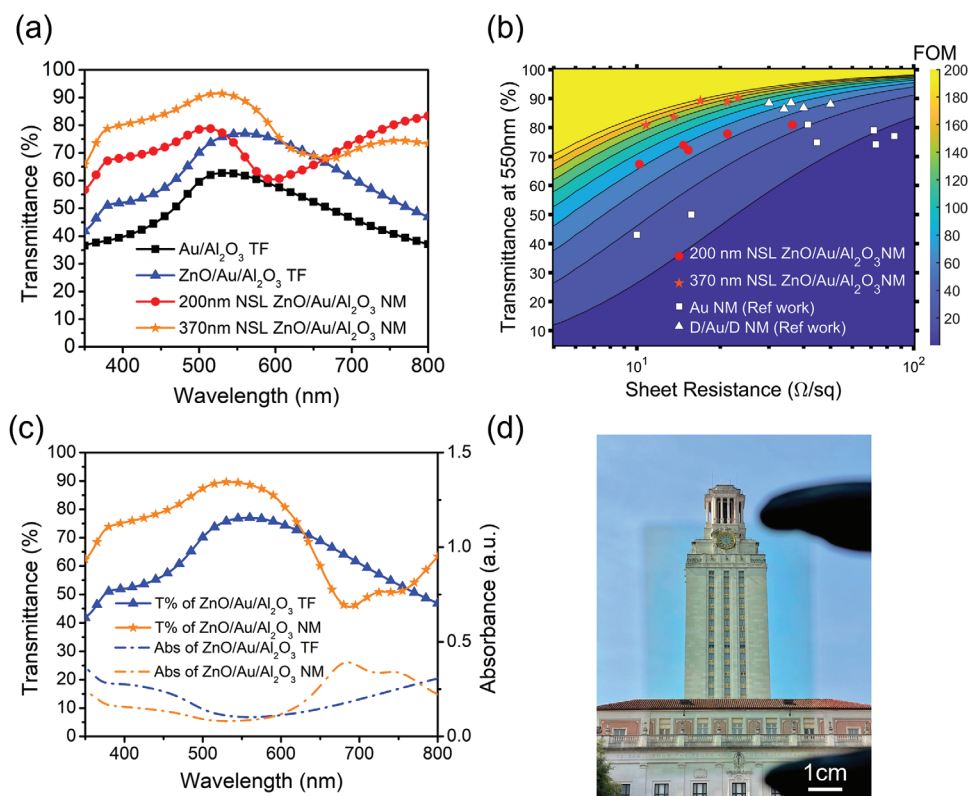
Figure 3. a) Transmittance spectra of Au/Al$_2$O$_3$ TF, ZnO/Au/Al$_2$O$_3$ TF, and the corresponding ZnO/Au/Al$_2$O$_3$ NM films based on 200 and 370 nm NSL. b) Comparisons of transmittance (at 550 nm), sheet resistance, and FOM of ZnO/Au/Al$_2$O$_3$ NM films based on 200 and 370 nm NSL in this work with Au NM and dielectric/Au/dielectric (D/Au/D) NM with similar aperture size from reference works (listed in Table S1, Supporting Information). c) Transmittance and absorption spectra of 370 nm ZnO/Au/Al$_2$O$_3$ TF and NM. d) Photograph of the 370 nm NSL ZnO/Au/Al$_2$O$_3$ NM films on the glass substrate.

2.2. Optoelectronic Properties and Figures of Merit of ZnO/Au/Al$_2$O$_3$ Nanomesh Films

The optical transmittance spectra of 200 and 370 nm based ZnO/Au/Al$_2$O$_3$ NM films are compared with those for Au/Al$_2$O$_3$ and ZnO/Au/Al$_2$O$_3$ thin films (TFs) in **Figure 3**a. For the most widely used figure of merit (FOM) for TCEs, the optical transmittance at 550 nm is employed as a measure of optical transparency.[25] The Au/Al$_2$O$_3$ and ZnO/Au/Al$_2$O$_3$ TFs have the same Au (15 nm) and Al$_2$O$_3$ (20 nm) thicknesses as the fabricated 200 and 370 nm based ZnO/Au/Al$_2$O$_3$ NM films. A significant increase in transmittance (at 550 nm) from 62.3% to 77.0% was observed for the ZnO/Au/Al$_2$O$_3$ TF after the addition of the top dielectric ZnO layer to Au/Al$_2$O$_3$ TF. This increase in transmittance can be attributed to the antireflective effect and suppression of surface plasmons in dielectric/metal/dielectric transparent conductors.[35] The 370 nm based ZnO/Au/Al$_2$O$_3$ NM film exhibited the highest transmittance at 550 nm of 90.1% while the 200 nm based ZnO/Au/Al$_2$O$_3$ NM film yielded a transmittance at 550 nm of 72.2%, owing to a substantial size reduction of the PS spheres in NSL for the 200 nm based NM films. The overall improvement in transmittance can be ascribed to the ZnO/Au/Al$_2$O$_3$ dielectric/metal/dielectric configuration which synergistically enhances the transmittance over the visible range (350–700 nm) by providing a major antireflective effect.

To quantitatively evaluate the performance of the metal NM films as TCEs, we use the FOM proposed by Dressel and Gruner[36] given by

$$\text{FOM} = \frac{\sigma_{\text{dc}}}{\sigma_{\text{opt}}} = \frac{188.5}{R_{\text{sheet}}\left(T_{550\,\text{nm}}^{-\frac{1}{2}} - 1\right)} \tag{1}$$

where σ_{dc} is the direct current conductivity, σ_{opt} is the optical conductivity in $\Omega^{-1}\text{cm}^{-1}$ at a wavelength of 550 nm, R_{sheet} is the sheet resistance in Ω sq^{-1}, and $T_{550\,\text{nm}}$ is the optical transmittance at 550 nm. This FOM aims to maximize the transmittance and minimize the sheet resistance for TCEs. However, maximizing the transmittance and minimizing sheet resistance requires a significant trade-off in metal NM films and one or the other therefore needs to be compromised.[37] Generally, a TCE film with a transmittance greater than 90% and sheet resistance less than 100 Ω sq^{-1} is required to meet the industrial standard, corresponding to a FOM of 35.[38] Figure 3b shows a contour map of FOM as a function of transmittance at 550 nm ($T_{550\,nm}$) and sheet resistance, with the corresponding values for our 200 and 370 nm based ZnO/Au/Al$_2$O$_3$ NM films, Au NM film (from reference work), and dielectric/Au/dielectric (D/Au/D) NM film with similar aperture size (from reference work listed in Table S1, Supporting Information). Transmittance spectra of samples with different O$_2$ etching time for

ADVANCED
SCIENCE NEWS
www.advancedsciencenews.com

ADVANCED
OPTICAL
MATERIALS
www.advopticalmat.de

370 nm based ZnO/Au/Al$_2$O$_3$ NM film are compared in Figure S1 (Supporting Information). The correlation between sheet resistance and transmittance was influenced by different O$_2$ etch time for both 200 and 370 nm based ZnO/Au/Al$_2$O$_3$ NM films, which is collectively summarized in Table S2 (Supporting Information). The 370 nm based ZnO/Au/Al$_2$O$_3$ NM film with a sheet resistance of 16.9 Ω sq^{-1} at a transmittance of 89.2% yields the best FOM value at 190.2. In contrast, the 200 nm based ZnO/Au/Al$_2$O$_3$ NM film with a sheet resistance of 10.2 Ω sq^{-1} and a transmittance of 67.4% results in FOM value of 84.6. This can be attributed to the higher metal coverage percentage (68.3%) in the 200 nm based ZnO/Au/Al$_2$O$_3$ NM film compared to that of the 370 nm based ZnO/Au/Al$_2$O$_3$ NM film (35.0%) resulting in high transmittance value. The corresponding transmittance, sheet resistance, and FOM value for 200 and 370 nm based ZnO/Au/Al$_2$O$_3$ NM films are summarized in Table S2 (Supporting Information). Based on the average performance of the 370 nm based ZnO/Au/Al$_2$O$_3$ NM films (see Figure 3b), our structures outperform the previously reported state-of-the-art Au NM and D/Au/D NM films.[24,25] Comparing the FOM value for our 370 nm based ZnO/Au/Al$_2$O$_3$ NM film (FOM = 190.2, $T_{550 nm}$= 89.2%, and R_{sheet} = 16.9 Ω sq^{-1}) to that of commercially available ITO (FOM ≈ 111.3, $T_{550 nm}$ ≈ 85%, and R_{sheet} ≈ 20 Ω sq^{-1}), we conclude that our NM films can serve as a potential alternative to ITO, including for applications requiring nonplanar or mechanically flexible form factors for which ITO is not well-suited (see Supporting Information, Figure S2).

Figure 3c shows the transmittance and absorption spectra of the 370 nm ZnO/Au/Al$_2$O$_3$ NM film and ZnO/Au/Al$_2$O$_3$ TF. The transmittance in the wavelength range of 350 nm to 620 nm is significantly enhanced in the case of 370 nm ZnO/Au/Al$_2$O$_3$ NM film as compared to that of the ZnO/Au/Al$_2$O$_3$ TF. However, a transmittance drop was observed at longer wavelengths (from 620 to 800 nm) for the 370 nm ZnO/Au/Al$_2$O$_3$ NM film due to the presence of distinct absorption peaks which are caused primarily by Au plasmonic resonances. Figure 3d shows a photograph of the fabricated 370 nm based ZnO/Au/Al$_2$O$_3$ NM film on a glass substrate with a dimension of 75 mm × 50 mm. The fabricated large, highly transparent NM film could open a pathway toward smart windows and related applications.

Computational modeling was performed on metal mesh structures to elucidate the physical mechanisms governing the optical properties of fabricated ZnO/Au/Al$_2$O$_3$ NM films. Simulations were carried out with commercial software (Synopsys, DiffractMOD) based on the rigorous coupled wave analysis (RCWA) method. **Figure 4**a shows the simulated (dashed line) and experimental (solid line) transmittance and absorption spectra of ZnO/Au/Al$_2$O$_3$ NM based on 370 nm-period NM structures, demonstrating good agreement between the optical characteristics of simulated and experimental structures. The geometric parameters for the structure simulated in Figure 4a are periodicity, aperture diameter, and thicknesses of Al$_2$O$_3$, Au and ZnO layers which are taken to be 370, 305, 20, 15, and 20 nm, respectively. Simulated results exhibited slight red shifts in both transmittance and absorption maxima compared to experimental results that may be attributed to an increase in effective periodicity owing to the larger polydispersity in the colloidal 370 nm diameter PS particle solutions. An increase
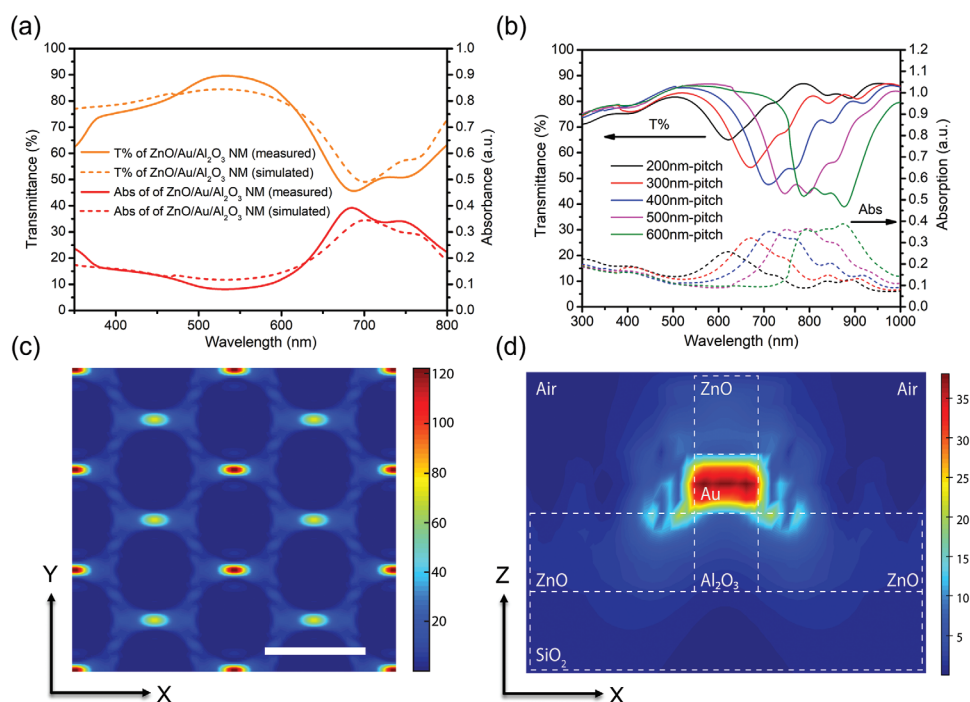

Figure 4. a) Measured and simulated transmittance and absorption spectra of ZnO/Au/Al$_2$O$_3$ NM films based on 370 nm NSL. b) Simulated transmittance and absorption spectra with different periodicities (200 nm to 600 nm) of ZnO/Au/Al$_2$O$_3$ NM films. c) In-plane (X–Y direction) electric field at incident wavelength of 700 nm for ZnO/Au/Al$_2$O$_3$ NM films based on 370 nm NSL. Inset scale bar represents 500 nm dimension size. d) Out-of-plane (X–Z direction) electric field at incident wavelength of 700 nm for ZnO/Au/Al$_2$O$_3$ NM films based on 370 nm NSL.

in effective periodicity will cause red-shifting of absorption maxima due to a complementary red-shift of plasmonic resonances supported by the periodic structures, as verified by periodicity dependent simulations. Simulated transmittance and absorption spectra of ZnO/Au/Al$_2$O$_3$ NM with different periodicities are shown in Figure 4b. To ensure accurate and comparable results across simulated NMs with varying periodicities, the fill factor (ratio of aperture area to metal coverage area) of simulated ZnO/Au/Al$_2$O$_3$ NMs was maintained at 1.6 which is the experimentally measured fill factor of our 370 nm NSL ZnO/Au/Al$_2$O$_3$ NM film. It is clear that increasing periodicity of ZnO/Au/Al$_2$O$_3$ NM results in larger red-shifting of absorption maxima from Figure 4b. The red-shifting of the absorption maxima also increases the bandwidth of high transmittance regions of NM films with larger periodicities. Maximum transmittance is sustained for almost the entire visible range for ZnO/Au/Al$_2$O$_3$ NM with periodicity >600 nm. While this may outline a path for higher transmittance for ZnO/Au/Al$_2$O$_3$ NM with applications relevant to the visible spectrum, it is important to note that devices with small carrier diffusion lengths such as organic semiconductors will have decreased electrical performance due to the increased electrode spacing and thus require NM with small periodicities.[39] Therefore, a pitch of 370 nm was chosen for ZnO/Au/Al$_2$O$_3$ NM to balance both the optical and electrical performance of our devices. Figure 4c,d demonstrate the in-plane (X–Y direction) and out-of-plane (X–Z direction) of the electric field amplitude of the simulated ZnO/Au/Al$_2$O$_3$ NM based on 370 nm NSL under monochromic illumination (at 700 nm) corresponding to the absorption maxima. The input light was normally incident on the simulated structure and the electric field was polarized along the Y-direction. As shown in Figure 4c,d, the electric field is strongly concentrated in the Au layer at the narrowest sections of the ZnO/Au/Al$_2$O$_3$ NM, which account for the largest parasitic absorption.

2.3. Application in Thermochromic Perovskite Smart Window

A large portion of energy consumption (50%) in buildings arises from heat transfer to buildings, specifically through windows due to solar illumination.[1] Energy-efficient thermochromic smart windows, which are composed of special materials that enable them to adjust light transmission dynamically based on the ambient temperature, can allow energy demand for building cooling to be reduced.[2] In recent years, halide perovskites have been considered as promising materials for thermochromic smart windows due to their switchable characteristics, including visible transparency and photovoltaic behavior, through phase transition between low and high temperatures.[3–5] While the thermochromic materials ideally respond to ambient heat from solar illumination, this heat can also be produced within smart windows by transparent heaters.[7] Transparent conductive oxides (TCOs) exhibit good performance as transparent heaters in terms of the trade-off between electrical conductivity and optical transparency in the visible range, their two main drawbacks concern their brittle nature and intrinsic low optical transmittance in the near-infrared (NIR) range due to plasmonic absorption.[40]

Based on our experimental results from Section 2.2, the 370 nm NSL ZnO/Au/Al$_2$O$_3$ NM films exhibited a clearly superior visible-wavelength optical transmittance compared to the ZnO/Au/Al$_2$O$_3$ TF. Moreover, the transmittance of ZnO/Au/Al$_2$O$_3$ NM in NIR range (800–2500 nm) showed an outstanding enhancement compared with ZnO/Au/Al$_2$O$_3$ TF (Figure S4, Supporting Information). The higher transmittance in NIR range of ZnO/Au/Al$_2$O$_3$ NM films could offer capability of adding another NIR modulation layer in the energy-efficient thermochromic smart windows to provide better heat modulation corresponding to different seasons.[41] Here, we use ZnO/Au/Al$_2$O$_3$ NM as an example to demonstrate the application in thermochromic smart windows. **Figure 5**a
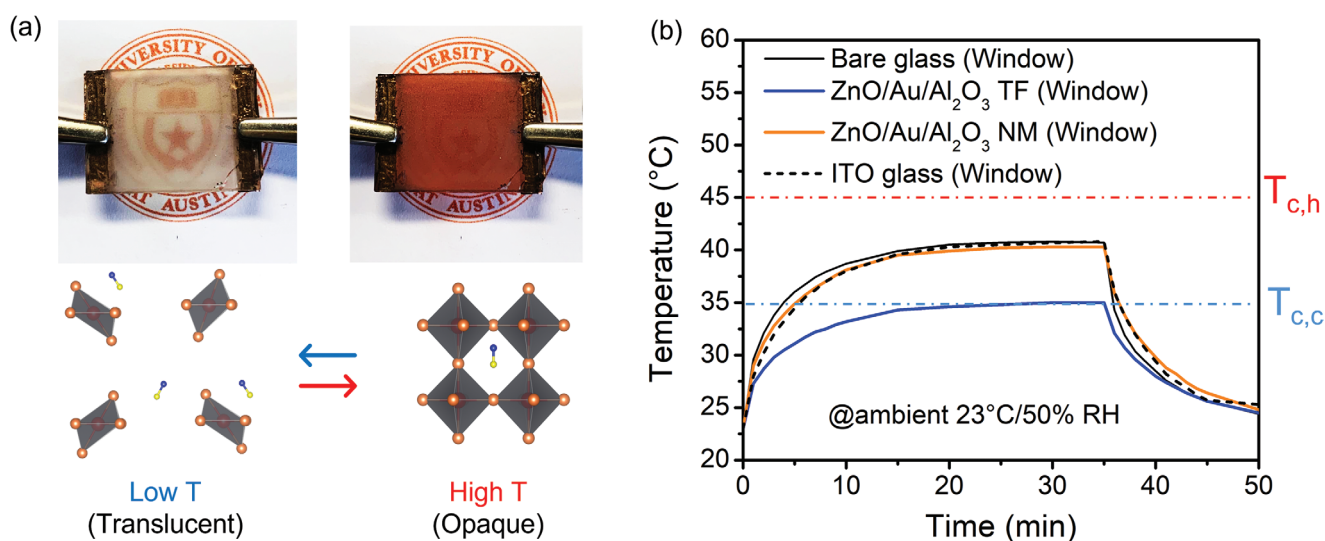

Figure 5. a) Photographs of TC-PVK smart windows integrated with ZnO/Au/Al$_2$O$_3$ NM films and schematics of cold-state to hot-state phase transition by heating and hot-state to cold-state transition by exposure to moisture. b) Temperature response curves of bare glass, ZnO/Au/Al$_2$O$_3$ TF, ZnO/Au/Al$_2$O$_3$ NM and ITO glass windows under AM 1.5G illumination. The ambient temperature is 23 °C.

shows a photograph of our ZnO/Au/Al$_2$O$_3$ NM film serving as transparent heater for a MAPbI$_{3-x}$Cl$_x$ TC-PVK smart window structure. The transparency of the TC-PVK layer is controlled by resistive heating of the ZnO/Au/Al$_2$O$_3$ NM film to increase the device temperature and therefore cause a structural transition of the TC-PVK layer to the optically opaque phase. Figure S3 (Supporting Information) shows X-ray diffraction spectra, confirming a significant phase transition from room temperature (nonperovskite phase, low T) to high temperature (perovskite phase, high T). At low temperature, MAPbI$_3$-based thermochromic perovskite converts to MA$_4$PbI$_6$·2H$_2$O due to its hydrophilic nature that readily absorbs water,[42,43] as hydrated MA$_4$PbI$_6$·2H$_2$O desorbs water and transforms to cubic phase of MAPbI$_3$ at high temperature.[44] These two phases can be reversibly switched in response to ambient temperature as illustrated in Figure 5a.

An essential factor to consider in the fabrication of thermochromic smart windows is the critical temperature for the thermochromic transition. Previous reports have demonstrated a transition temperature of >50 °C for hydrated MAPbI$_3$ perovskite thermochromic smart windows.[2] However, the reported high transition temperature limits the utilization of TC-PVK smart windows in real-life applications since the typical window temperature normally does not reach 50 °C even in the summer. To evaluate the photothermal behavior of our ZnO/Au/Al$_2$O$_3$ NM, we constructed an enclosure with double-glazed window structure to monitor the change in surface temperature under an AM 1.5G solar simulator (see Figure S5, Supporting Information). The resulting temperature as a function of time for bare glass, ZnO/Au/Al$_2$O$_3$ TF, ZnO/Au/Al$_2$O$_3$ NM, and ITO glass were systematically recorded (see Figure 5b). The surface temperature of the bare glass, ZnO/Au/Al$_2$O$_3$ TF, ZnO/Au/Al$_2$O$_3$ NM, and ITO glass reached steady state at 40.5, 34.6, 39.9, and 40.3 °C, respectively, in 20 min (ambient conditions were T = 23 °C and relative humidity of 50%). The temperature indicates that an external heating source is required to

activate the thermochromism of TC-PVK smart windows under standard solar illumination.

To address this requirement, we constructed a switchable TC-PVK smart window structure consisting of a TC-PVK layer integrated with ZnO/Au/Al$_2$O$_3$ NM (dimension of 20 mm × 15 mm) with an external heating source as illustrated in the inset of **Figure 6**a. The TC-PVK layer was prepared based on the fabrication process of reference[2] and was spin-coated on the opposite side of the ZnO/Au/Al$_2$O$_3$ NM window. Two bus bar copper electrodes were attached on top of the ZnO/Au/Al$_2$O$_3$ NM film to conduct electricity from an external power supply. The power required for the TC-PVK with ZnO/Au/Al$_2$O$_3$ NM was compared to that for the control sample of TC-PVK with ZnO/Au/Al$_2$O$_3$ TF to reach a target temperature of 50 °C (T_{target} = 50 °C) (see Figure 6a). The power consumption of the TC-PVK with ZnO/Au/Al$_2$O$_3$ TF, TC-PVK with ZnO/Au/Al$_2$O$_3$ NM, and ITO glass is 0.54, 0.496, and 0.66 W, respectively, indicating that the TC-PVK with ZnO/Au/Al$_2$O$_3$ NM required the lowest power consumption compared with TC-PVK with ZnO/Au/Al$_2$O$_3$ TF and TC-PVK with ITO glass samples.

A real-time transmittance setup was built to monitor the transmittance-time response of the TC-PVK smart window integrated with ZnO/Au/Al$_2$O$_3$ TF, ZnO/Au/Al$_2$O$_3$ NM, and ITO glass while resistive heating power is switched on and off (see Figure S6, Supporting Information). Figure 6b shows the transmittance-time response curves revealing thermochromic behavior of the TC-PVK smart window integrated with ZnO/Au/Al$_2$O$_3$ TF and ZnO/Au/Al$_2$O$_3$ NM under electrical heating, without (top plot) and with (bottom plot) AM 1.5G illumination. Real-time transmittance measurements, without and with solar illumination, reveal that while transient resistive heating is required to induce the thermochromic transition to the opaque state, standard solar illumination without additional heating is sufficient to maintain the opaque state. The heating parameters and optical properties of TC-PVK with ZnO/Au/Al$_2$O$_3$ TF, TC-PVK with ZnO/Au/Al$_2$O$_3$ NM, and TC-PVK with ITO glass
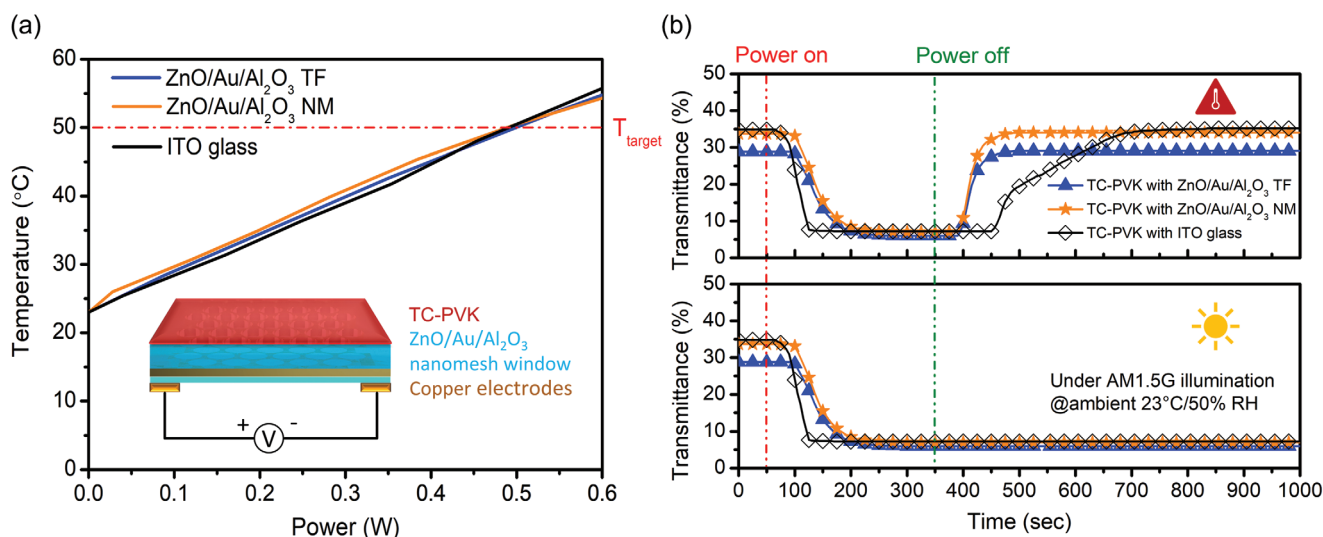

Figure 6. a) Electric heating test of ZnO/Au/Al$_2$O$_3$ TF, ZnO/Au/Al$_2$O$_3$ NM and ITO glasses for TC-PVK smart windows. The inset shows the corresponding device configuration of TC-PVK smart windows. b) Transmittance-time response curves for thermochromic behavior of TC-PVK smart windows integrated with ZnO/Au/Al$_2$O$_3$ TF, ZnO/Au/Al$_2$O$_3$ NM, and ITO glasses under electrical heating, without (top plot) and with (bottom plot) AM 1.5G illumination. The dashed lines show the timing for electric heat power on (red dashed line) and power off (green dashed line).

Table 1. Heating parameters and optical properties of TC-PVK windows integrated with ZnO/Au/Al$_2$O$_3$ TF, ZnO/Au/Al$_2$O$_3$ NM and ITO glasses.

Sample	Voltage [V]	Current [A]	Power [W]	$\tau_{lum,cold}$ [%]	$\tau_{lum,hot}$ [%]
TC-PVK on ZnO/Au/Al$_2$O$_3$ TF glass	2.5	0.216	0.540	28.8	5.9
TC-PVK on ZnO/Au/Al$_2$O$_3$ NM glass	4	0.124	0.496	33.7	7.0
TC-PVK on ITO glass	4	0.165	0.660	35.4	8.5

are summarized in **Table 1**. In Figure 6b, the average transmittance in the visible wavelength range (380–760 nm) under electrical heating was 28.8%, 33.7%, and 35.4% for the TC-PVK with ZnO/Au/Al$_2$O$_3$ TF, TC-PVK with ZnO/Au/Al$_2$O$_3$ NM, and TC-PVK with ITO glass, respectively in the translucent state (low T). The average transmittance value in the opaque state (high T) was 5.9%, 7.0%, and 8.5% for ZnO/Au/Al$_2$O$_3$ TF, TC-PVK with ZnO/Au/Al$_2$O$_3$ NM, and TC-PVK with ITO glass, respectively (see top figure of Figure 6b). The difference in average transmittance in both low T and high T states can be ascribed to the transmittance difference in visible wavelength range of ZnO/Au/Al$_2$O$_3$ TF, ZnO/Au/Al$_2$O$_3$ NM, and ITO glass. The transition time from low T to high T for the above-mentioned samples is ≈4 min to reach steady opaque state. Notably, the transition time from high T to low T for TC-PVK with ITO glass was 60s longer than the other two samples. This is most likely due to the excellent thermal conductivity of Au (310 W m^{-1} K^{-1}) thin film that efficiently dissipates the heat from the surface as compared to the much lower thermal conductivity of ITO (0.84 W m^{-1} K^{-1}) that likely results in slower heat dissipation.[45,46] Finally, the TC-PVK smart window with the integrated ZnO/Au/Al$_2$O$_3$ NM film was first heat-activated to induce the phase transition to occur at high T, and solar illumination was then applied to consistently maintain its low transmittance over time with the heating power shut-off (see bottom figure of Figure 6b). The observed consistency in transmittance over time can be attributed to the stable high-temperature perovskite phase, wherein the perovskite layer with a small bandgap absorbs a broad spectrum of photons from solar irradiation.[47]

3. Conclusion

In summary, ZnO/Au/Al$_2$O$_3$ NM films with periodicities of 200 and 370 nm have been fabricated using NSL. The experimental results demonstrated that the ZnO/Au/Al$_2$O$_3$ NM film with a periodicity of 370 nm exhibited a transmittance over 90% at 550 nm and sheet resistance lower than 20 Ω sq^{-1}. This structure yields a standard FOM of over 190 which is superior to the current state-of-the-art TCEs, opening new pathways toward its application in many optoelectronic devices. We further demonstrated smart window structures based on highly conductive, transparent ZnO/Au/Al$_2$O$_3$ NM and TC-PVK films. The transparency of the developed structure was manipulated by transient resistive heating to trigger a thermochromic transition to an opaque state that can be maintained solely by 1-sun, AM

1.5 G illumination. Thus, the developed climate-adaptive, low power-activated, and fast-switching smart window structure could be beneficial for the next generation of perovskite-based smart photovoltaic windows.

4. Experimental Section

Materials: Nonfunctionalized PS particles were purchased from Polysciences Inc. 200 proof ethanol was purchased from Sigma Aldrich. Chemicals and nanoparticles were used as received from the manufacturer. Particles used in this experiment were 200 and 370 nm in diameter with 2.5 and 4% coefficient of variation, respectively. Both 200 and 370 nm nanoparticles were 2.5 w/v % concentration. Self-assembling colloidal nanoparticle solutions used to lithographically define the NMs were made from a 1:1 volume ratio of nanoparticle solution and ethanol.

Fabrication of ZnO/Au/Al$_2$O$_3$ Nanomesh Films: First, the glass substrates were thoroughly cleaned using a sequential sonication process with acetone, methanol, and deionized water. Then, the glass substrates were immersed in water which is contained in a 3D printed drop cast. PS spheres (≈200 and ≈370 nm) were sequentially injected at the air–water interface, creating a self-assembled monolayer of spherical particles. After that, the water in the drop cast was drained, allowing the monolayer to be deposited on the glass substrates. Then, the glass substrates were air dried at room temperature for 24 h, creating a hexagonal close packed pattern of PS spheres on glass substrates. Next, with the PS spheres as soft lithography masks, the substrates were etched under O$_2$ plasma in a reactive ion etcher (RIE, Oxford Instruments) to reduce the PS size and open the gaps in between particles to expose the glass area. Subsequently, Al$_2$O$_3$ (≈20 nm) and Au (≈15 nm) were deposited on the substrates using e-beam evaporator (CHA Industries), with a base chamber pressure of 5 × 10^{-6} Torr and deposition rate of 1 Å s^{-1}. After that, the PS spheres were lifted off the substrates using a sonication process with toluene for 10 min. Then, the substrates were treated with UV-Ozone to improve the wettability for the sequential zinc oxide (ZnO) sol–gel spin coating process. Finally, the substrates were annealed on the hot plate at 200 °C for 30 min.

Fabrication of ZnO/Au/Al$_2$O$_3$ Thin Films: For the fabrication of ZnO/Au/Al$_2$O$_3$ TFs, the glass substrates were first cleaned using the standard cleaning procedure as described in the previous section. A thin layer of Al$_2$O$_3$ (≈20 nm) and Au (≈15 nm) were deposited on the glass substrates using e-beam evaporator (CHA Industries), with chamber pressure of 5 × 10^{-6} Torr and deposition rate of 1 Å s^{-1}. After the evaporation process, the substrates were treated with UV-Ozone to improve the wettability of the substrates. Subsequently, sol-gel processed ZnO, which was synthesized as described in the previous report,[29] was spin coated on the substrates. Afterwards, the final substrates were annealed at 200 °C for 30 min.

Device Characterization: The surface morphology and topography of the fabricated ZnO/Au/Al$_2$O$_3$ NM films were investigated using scanning electron microscope (SEM Zeiss Neon 40) and atomic force microscope (AFM Bruker Icon), respectively. The crystallinity of the perovskite used for thermochromic device was studied using X-ray Diffraction (XRD, Rigaku Miniflex 600 Diffractometer). The sheet resistance measurements were carried out using a four-point probe system (Ossila Ltd). The absorption and transmittance spectra were measured using a UV–visible spectrometer (Cary 5000 UV/Vis NIR). Electric heating test for ZnO/Au/Al$_2$O$_3$ TF, and ZnO/Au/Al$_2$O$_3$ NM samples were carried out by connecting to the external power supply (Caswell, NSP-2050) and a thermocouple with a K-type sensor probe was used to record the window temperature. The temperature response of different window layers (bare glass, ZnO/Au/Al$_2$O$_3$ TF, and ZnO/Au/Al$_2$O$_3$ NM) under AM 1.5G illumination was conducted with a solar simulator (Newport LCS-100) at ambient temperature 23 °C. For the measurements of average transmittance (380–760 nm) determining thermochromic behavior, a transmission meter (LS162, Linshang) was used.

**ADVANCED
SCIENCE NEWS**

www.advancedsciencenews.com

**ADVANCED
OPTICAL
MATERIALS**

www.advopticalmat.de

Simulations of Transmittance and Absorption Spectra: Simulated transmittance and absorption spectra were carried out with Synopsys, DiffractMOD model using a 3D model based on ZnO/Au/Al$_2$O$_3$ NM configurations. Periodicity, aperture diameter, and thicknesses of Al$_2$O$_3$, Au and ZnO layers were defined as 370, 305, 20, 15, and 20 nm, respectively. The background was set to air ($n = 1$) and SiO$_2$ was used as substrate material. The refractive index of the SiO$_2$ was obtained from DiffractMOD material database. The refractive index of Al$_2$O$_3$, Au, and ZnO was obtained from references.[48–50]

Fabrication of Thermochromic Perovskite Smart Windows: The sample fabrication was conducted in a nitrogen-filled glove box (water content ≤ 1 ppm, oxygen content ≤ 1 ppm). CH$_3$NH$_3$I (MAI, >99.0%) was purchased from TCI America. PbCl$_2$ (99%), PbI$_2$ (99%) and DMF (anhydrous, 99.8%) were purchased from Sigma–Aldrich. ITO glass substrates (20 Ω sq^{-1}) were purchase from Ossila Ltd. The MAPbI$_{3-x}$Cl$_x$ thermochromic perovskite precursor was prepared based on the reference work.[2] Briefly, 6.5 M MAI and 1 M PbCl$_2$ were dissolved in DMF solvent, respectively and stirred at 50 °C for 1 h to ensure the dissolution was complete. The ZnO/Au/Al$_2$O$_3$ TF, ZnO/Au/Al$_2$O$_3$ NM, and ITO glass substrates were treated with UV-Ozone cleaner for 20 min before transferred to glove box. The MAPbI$_{3-x}$Cl$_x$ precursor solution was then spin-coated on the glass substrates at 2000 rpm for 30 s and sequentially annealed on a hot plate at 100 °C for 1 h to facilitate crystallization of perovskite layer.

Supporting Information

Supporting Information is available from the Wiley Online Library or from the author.

Conflict of Interest

The authors declare no conflict of interest.

Data Availability Statement

The data that support the findings of this study are available from the corresponding author upon reasonable request.

[1] L. Long, H. Ye, *Sci. Rep.* **2014**, *4*, 6427.

[2] S. Liu, Y. W. Du, C. Y. Tso, H. H. Lee, R. Cheng, S.-P. Feng, K. M. Yu, *Adv. Funct. Mater.* **2021**, *31*, 2010426.

[3] M. De Bastiani, M. I. Saidaminov, I. Dursun, L. Sinatra, W. Peng, U. Buttner, O. F. Mohammed, O. M. Bakr, *Chem. Mater.* **2017**, *29*, 3367.

[4] B. A. Rosales, L. E. Mundt, T. G. Allen, D. T. Moore, K. J. Prince, C. A. Wolden, G. Rumbles, L. T. Schelhas, L. M. Wheeler, *Nat. Commun.* **2020**, *11*, 5234.

[5] J. Lin, M. Lai, L. Dou, C. S. Kley, H. Chen, F. Peng, J. Sun, D. Lu, S. A. Hawks, C. Xie, F. Cui, A. P. Alivisatos, D. T. Limmer, P. Yang, *Nat. Mater.* **2018**, *17*, 261.

[6] C. Celle, C. Mayousse, E. Moreau, H. Basti, A. Carella, J.-P. Simonato, *Nano Res.* **2012**, *5*, 427.

[7] L. Veeramuthu, B.-Y. Chen, C.-Y. Tsai, F.-C. Liang, M. Venkatesan, D.-H. Jiang, C.-W. Chen, X. Cai, C.-C. Kuo, *RSC Adv.* **2019**, *9*, 35786.

[8] D. S. Hecht, L. Hu, G. Irvin, *Adv. Mater.* **2011**, *23*, 1482.

[9] T.-R. Zhang, Y.-N. Wang, Y.-F. Liu, J. Feng, *Appl. Phys. Lett.* **2022**, *120*, 051106.

[10] H. B. Lee, W.-Y. Jin, M. M. Ovhal, N. Kumar, J.-W. Kang, *J. Mater. Chem. C* **2019**, *7*, 1087.

[11] H. Chang, G. Wang, A. Yang, X. Tao, X. Liu, Y. Shen, Z. Zheng, *Adv. Funct. Mater.* **2010**, *20*, 2893.

[12] L. Hu, D. S. Hecht, G. Grüner, *Nano Lett.* **2004**, *4*, 2513.

[13] J. Kvavle, S. Schultz, R. Selfridge, *Appl. Opt.* **2009**, *48*, 5280.

[14] S. De, T. M. Higgins, P. E. Lyons, E. M. Doherty, P. N. Nirmalraj, W. J. Blau, J. J. Boland, J. N. Coleman, *ACS Nano* **2009**, *3*, 1767.

[15] T. Qiu, B. Luo, F. Ali, E. Jaatinen, L. Wang, H. Wang, *ACS Appl. Mater. Interfaces* **2016**, *8*, 22768.

[16] T. Qiu, E. M. Akinoglu, B. Luo, M. Giersig, M. Liang, J. Ning, L. Zhi, *Part. Part. Syst. Charact.* **2017**, *34*, 1600262.

[17] T. Qiu, E. M. Akinoglu, B. Luo, M. Konarova, J.-H. Yun, I. R. Gentle, L. Wang, *Adv. Mater.* **2022**, *34*, 2103842.

[18] X. Lu, Y. Zhang, Z. Zheng, *Adv. Electron. Mater.* **2021**, *7*, 2001121.

[19] C. Stelling, C. R. Singh, M. Karg, T. A. F. König, M. Thelakkat, M. Retsch, *Sci. Rep.* **2017**, *7*, 42530.

[20] M. Parchine, J. McGrath, M. Bardosova, M. E. Pemble, *Langmuir* **2016**, *32*, 5862.

[21] M. Parchine, T. Kohoutek, M. Bardosova, M. E. Pemble, *Sol. Energy Mater. Sol. Cells* **2018**, *185*, 158.

[22] P. Gao, J. He, S. Zhou, X. Yang, S. Li, J. Sheng, D. Wang, T. Yu, J. Ye, Y. Cui, *Nano Lett.* **2015**, *15*, 4591.

[23] G. Cossio, E. T. Yu, *Nano Lett.* **2020**, *20*, 5090.

[24] K. Bley, J. Semmler, M. Rey, C. Zhao, N. Martic, R. N. K. Taylor, M. Stingl, N. Vogel, *Adv. Funct. Mater.* **2018**, *28*, 1706965.

[25] T. Qiu, B. Luo, E. M. Akinoglu, J.-H. Yun, I. R. Gentle, L. Wang, *Adv. Funct. Mater.* **2020**, *30*, 2002556.

[26] S.-W. Lee, S. Kim, S. Bae, K. Cho, T. Chung, L. E. Mundt, S. Lee, S. Park, H. Park, M. C. Schubert, S. W. Glunz, Y. Ko, Y. Jun, Y. Kang, H.-S. Lee, D. Kim, *Sci. Rep.* **2016**, *6*, 38150.

[27] T. Chen, J. Xie, P. Gao, *Adv. Energy Sustainability Res.* **2022**, *3*, 2100218.

[28] N. N. Shlenskaya, N. A. Belich, M. Grätzel, E. A. Goodilin, A. B. Tarasov, *J. Mater. Chem. A* **2018**, *6*, 1780.

[29] S.-H. Wu, M.-Y. Lin, S.-H. Chang, W.-C. Tu, C.-W. Chu, Y.-C. Chang, *J. Phys. Chem. C* **2018**, *122*, 236.

[30] Z. Wang, Z. Zhang, L. Xie, S. Wang, C. Yang, C. Fang, F. Hao, *Adv. Opt. Mater.* **2022**, *10*, 2101822.

[31] T. Leijtens, G. E. Eperon, S. Pathak, A. Abate, M. M. Lee, H. J. Snaith, *Nat. Commun.* **2013**, *4*, 2885.

[32] M. Spalla, E. Planes, L. Perrin, M. Matheron, S. Berson, L. Flandin, *ACS Appl. Energy Mater.* **2019**, *2*, 7183.

[33] E. M. Akinoglu, A. J. Morfa, M. Giersig, *Langmuir* **2014**, *30*, 12354.

[34] Y.-G. Bi, Y.-F. Liu, X.-L. Zhang, D. Yin, W.-Q. Wang, J. Feng, H.-B. Sun, *Adv. Opt. Mater.* **2019**, *7*, 1800778.

[35] M. K. Hedayati, M. Elbahri, *Materials* **2016**, *9*, 497.

[36] M. Dressel, G. Grüner, *Electrodynamics of Solids: Optical Properties of Electrons in Matter*, Cambridge University Press, Cambridge **2002**.

[37] A. Anand, M. M. Islam, R. Meitzner, U. S. Schubert, H. Hoppe, *Adv. Energy Mater.* **2021**, *11*, 2100875.

[38] C. Zhang, B. Anasori, A. Seral-Ascaso, S.-H. Park, N. McEvoy, A. Shmeliov, G. S. Duesberg, J. N. Coleman, Y. Gogotsi, V. Nicolosi, *Adv. Mater.* **2017**, *29*, 1702678.

[39] D. Chen, G. Fan, H. Zhang, L. Zhou, W. Zhu, H. Xi, H. Dong, S. Pang, X. He, Z. Lin, J. Zhang, C. Zhang, Y. Hao, *Nanomaterials* **2019**, *9*, 932.

[40] D. T. Papanastasiou, A. Schultheiss, D. Muñoz-Rojas, C. Celle, A. Carella, J.-P. Simonato, D. Bellet, *Adv. Funct. Mater.* **2020**, *30*, 1910225.

[41] S. Wang, Y. Zhou, T. Jiang, R. Yang, G. Tan, Y. Long, *Nano Energy* **2021**, *89*, 106440.

[42] S. Foo, M. Thambidurai, P. S. Kumar, R. Yuvakkumar, Y. Huang, C. Dang, *Int. J. Energy Res.* **2022**, *46*, 21441.

[43] A. Halder, D. Choudhury, S. Ghosh, A. S. Subbiah, S. K. Sarkar, *J. Phys. Chem. Lett.* **2015**, *6*, 3180.

[44] Y. Zhang, C. Y. Tso, J. S. Iñigo, S. Liu, H. Miyazaki, C. Y. H. Chao, K. M. Yu, *Appl. Energy* **2019**, *254*, 113690.

[45] J. Carvill (Ed: J. Carvill), *Mechanical Engineer's Data Handbook*, Butterworth-Heinemann, Oxford **1993**.

[46] L. Wang, J. Wen, C. Yang, B. Xiong, *Sci. Technol. Adv. Mater.* **2018**, *19*, 791.

[47] S. Liu, Y. Li, Y. Wang, K. M. Yu, B. Huang, C. Y. Tso, *Adv. Sci.* **2022**, *9*, 2106090.

[48] R. Boidin, T. Halenkovič, V. Nazabal, L. Beneš, P. Němec, *Ceram. Int.* **2016**, *42*, 1177.

[49] D. I. Yakubovsky, Y. V. Stebunov, R. V. Kirtaev, G. A. Ermolaev, M. S. Mironov, S. M. Novikov, A. V. Arsenin, V. S. Volkov, *Adv. Mater. Interfaces* **2019**, *6*, 1900196.

[50] O. Aguilar, S. de Castro, M. P. F. Godoy, M. Rebello Sousa Dias, *Opt. Mater. Express* **2019**, *9*, 3638.